Revealing the flux: Using processed Husimi maps to visualize dynamics of bound systems and mesoscopic transport

Douglas J. Mason
Department of Physics, Harvard University, Cambridge, Massachusetts 02138, USA

Mario F. Borunda*
Department of Physics, Oklahoma State University, Stillwater, Oklahoma 74078, USA

Eric J. Heller
Department of Physics and Department of Chemistry and Chemical Biology, Harvard University, Cambridge, Massachusetts 02138, USA

(Received 29 December 2014; revised manuscript received 18 March 2015; published 8 April 2015)

We elaborate upon the "processed Husimi map" representation for visualizing quantum wave functions using coherent states as a measurement of the local phase space to produce a vector field related to the probability flux. Adapted from the Husimi projection, the processed Husimi map is mathematically related to the flux operator under certain limits but offers a robust and flexible alternative since it can operate away from these limits and in systems that exhibit zero flux. The processed Husimi map is further capable of revealing the full classical dynamics underlying a quantum wave function since it reverse engineers the wave function to yield the underlying classical ray structure. We demonstrate the capabilities of processed Husimi maps on bound systems with and without electromagnetic fields, as well as on open systems on and off resonance, to examine the relationship between closed system eigenstates and mesoscopic transport.

DOI: 10.1103/PhysRevB.91.165405 PACS number(s): 03.65.Sq, 03.65.Ta, 07.05.Rm

I. INTRODUCTION

In Mason *et al.* [1], we introduced the "processed Husimi map," which extends the concept of the probability flux, or probability current $\mathbf{j}(\mathbf{r},\mathbf{p})$, defined as

$$\hat{\mathbf{j}}_{\mathbf{r}} = \frac{1}{2m}(|\mathbf{r}\rangle\langle\mathbf{r}|\hat{\mathbf{p}} + \hat{\mathbf{p}}|\mathbf{r}\rangle\langle\mathbf{r}|), \tag{1}$$

where m is the mass of a particle in the system, $\mathbf{r}$ is the position and $\hat{\mathbf{p}}$ is the momentum operator.

One of the limitations of the probability flux is that it vanishes on stationary states for systems with time-reversal symmetry making it impossible to reveal the strong semiclassical connections between trajectory flow and quantum eigenstate. Consider the stadium billiard presented in Fig. 1. This wave function exhibits the strong influence of classical orbits and is known as a scarred eigenstate [2]. For this bound system, the flux is always zero. Unless the system is coupled to a continuum, the flux as a tool for examining the system dynamics provides no information, even though information about the dynamics clearly exists before the coupling. The main goal of this article is to describe in detail algorithms that render processed Husimi maps, a numerical technique that is able to extract the information present in the system but to which the probability current is blind.

The processed Husimi map addresses the problem of the underlying dynamics encoded in stationary states by extending the definition of the flux to coherent state projections, also known as Husimi projections [3]. Applying several Husimi projections, each with a different momentum direction, at each location, it is possible to render the classical rays associated with a position and extract semiclassical paths from a quantum wave function even when the flux is zero. Husimi projections sampled across a system produce a Husimi *map*. By processing Husimi maps using the methods outlined in Mason *et al.* [1], we can show the locations and directions of classical trajectories suggested by a wave function. This technique has been used to examine the relationship between graphene boundary types and the classical dynamics of quasiparticles in each valley of the honeycomb dispersion relation, studying states with energies both close to and far from the Dirac point [4]. Although the processed Husumi approach was presented in summary before [1], the level of detail might be insufficient to allow nonexperts to develop their own programs. Here, we also introduce new mappings that quantify how boundaries and external fields affect those trajectories. In this paper, we also present a complete discussion of the results summarized previously and demonstrate the processing of Husimi maps on a wider variety of systems with and without external fields. In particular, we show how to use processed Husimi maps to interpret flux through open devices and mesoscopic devices.

II. THE PROCESSED HUSIMI MAP

The properties of coherent states make them a suitable basis for expanding the flux operator to a measurable definition, which we call the Husimi function [3]. It is defined as a measurement of a wave function $\psi(\mathbf{r})$ by a coherent state, or "test wave packet," written as

$$\mathrm{Hu}(\mathbf{r}_0,\mathbf{k}_0,\sigma;\psi(\mathbf{r})) = |\langle\psi|\mathbf{r}_0,\mathbf{k}_0,\sigma\rangle|^2, \tag{2}$$

where the parameter σ defines the spatial spread of the coherent state and defines the uncertainties is space and momentum. Weighting each of these measurements by the wave vector produces a Husimi vector; plotting all Husimi vectors at a point produces the full Husimi projection.

*mario.borunda@okstate.edu

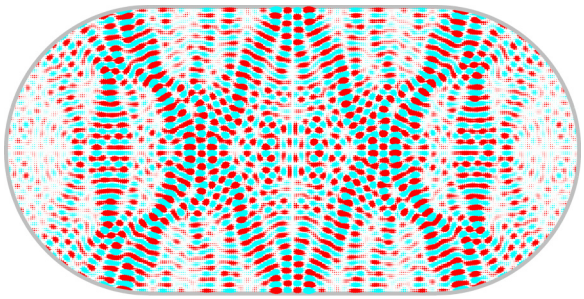

FIG. 1. (Color online) A scarred eigenstate of the stadium billiard reveals the strong influence of periodic classical orbits. The traditional flux provides no information: it is uniformly zero inside the billiard.

In this paper, we examine three approaches for processing the Husimi projection. The first approach utilizes the algorithm outlined in Mason *et al.* [1], which simplifies the full Husimi projection at each point, to give rise to the significant classical paths within the system. The second approach, which we describe in Sec. III C, identifies key points where the system boundary deflects straight classical paths, giving rise to the structure of the quantum wave function. The third approach sums all Husimi vectors at each point in space, indicating the net flow of classical paths at each point, and resulting in the vector-valued Husimi flux. The Husimi flux has parallels to the traditional flux, which we describe here.

Because of the large momentum uncertainty for small σ, coherent state projections merely reproduce the probability amplitude $|\psi(\mathbf{r})|^2$ in all directions of $\mathbf{k}_0$. The flux emerges as a small residual, which can be retrieved by summing each coherent state projection weighted by $\mathbf{k}_0$. We call this quantity the vector-valued Husimi flux,

$$\mathbf{Hu}(\mathbf{r}_0,\sigma;\psi(\mathbf{r})) = \int \mathbf{k}_0 |\langle\psi|\mathbf{r}_0,\mathbf{k}_0,\sigma\rangle|^2 d^d k_0. \tag{3}$$

Several of the results in these paper display sets of Husimi vectors for 32 equally spaced points in k space at each point in the system. We plot such sets of Husimi vectors at many points along a system, mapping the local phase space of the wave function. These visualizations are known as "Husimi maps" [3,5–7]. We refer to the maps that present the complete set of Husimi vectors at each point as *raw* Husimi maps.

In Appendix A, we show that as $\sigma \to 0$, the contributing points in the integral over k space reduce to just the orthogonal directions. In this limit, we can write the Husimi flux as

$$\lim_{\sigma\to 0} \mathbf{Hu}(\mathbf{r}_0,\sigma;\psi(\mathbf{r})) \propto \sum_{i=1}^{d} \mathbf{e}_i [|\langle\psi|\mathbf{r}_0,k_0\mathbf{e}_i,\sigma\rangle|^2 - |\langle\psi|\mathbf{r}_0,-k_0\mathbf{e}_i,\sigma\rangle|^2], \tag{4}$$

where $\mathbf{e}_i$ is the unit vector along the i^{th} orthogonal direction, and we sum over d dimensions. As presented in Ref. [1], both sides of Eq. (4) are proportional to the traditional flux measured at point $\mathbf{r}_0$ so that

$$\langle\psi|\hat{\mathbf{j}}_{\mathbf{r}_0}|\psi\rangle \propto \lim_{\sigma\to 0} \mathbf{Hu}(\mathbf{r}_0,\sigma;\psi). \tag{5}$$

For larger σ, reduced momentum uncertainty allows for substantial variation in the coherent state projections between different directions of $\mathbf{k}_0$. The reduced momentum uncertainty for larger coherent states also reduces spatial resolution. In the intermediate regime, we can use Husimi projections to map the local phase space of a wave function. By selecting an appropriate value for σ and taking snapshots of the local phase space at many points across a system, we can produce a clear map of the classical trajectories that correspond to a given wave function. Like the traditional flux map, Husimi maps can be integrated over lines and surfaces to reveal the total probability flux current.

The raw Husimi maps present snapshots of the phase space along the system. We can process the results to produce a semiclassical map exposing the dominant classical paths contributing to a given wave function. Thus the term *processed* Husimi map [1].

A question arises regarding the handling of boundaries in the system, beyond which the wave function goes to zero. Our definition reduces the magnitude of Husimi projections within distance σ of the boundary. When a coherent state interacts with a boundary, an image wave packet moving in the opposite direction can replace the boundary. On a curved boundary, a superposition of reflected image wave packets can be found that gives zero along a section of the curve. In both cases, reflections off the boundary amount to scattering between wave packets with different wave vectors. Thus the reduction in the Husimi projections near the boundaries is the result of wave packet scattering, making it possible to process Husimi maps to compute scattering metrics along the boundary, such as angular deflection presented in Sec. III C.

III. HUSIMI MAPS IN CLOSED SYSTEMS

A. Eigenstates of the circular system

The circular well is an ideal system for demonstrating the power of processing the Husimi map since its classical dynamics are simple and can be analytically determined. The Schrödinger equation in radial form is

$$\frac{d^2R(r)}{dr^2} + \frac{1}{r}\frac{dR(r)}{dr} + \left(k^2 - \frac{m^2}{r^2}\right)R(r) = 0. \tag{6}$$

Solutions to this equation are simultaneous eigenstates of energy and angular momentum, and thus n (number of nodes in the radial direction) and m (number of angular nodes) are good quantum numbers. Figures 2(a)–2(c) shows three such states, the first with $n = 0$, the second with $n \gg m$, and the third with $n \approx m$. The processed Husimi map in each shows the clear distinction between angular and radial components of the wave function, and how they correlate with classical paths with similar properties (further discussion of the classical correspondence can be found in Ref. [8]).

To examine the harmonic oscillator state in Fig. 2(d), the Husimi projection at each point must be modified. For the circular well, the dispersion relation is $\hbar k = \sqrt{2mE}$. However, due to the harmonic potential, the dispersion relation changes to $\hbar k(\mathbf{r}) = \sqrt{2m(E - V(\mathbf{r}))}$. This means that a different sweep in k space must be made at each point to produce an accurate Husimi map. Figure 2(d) shows such a state with $V(\mathbf{r}) = V_0 r^2$.

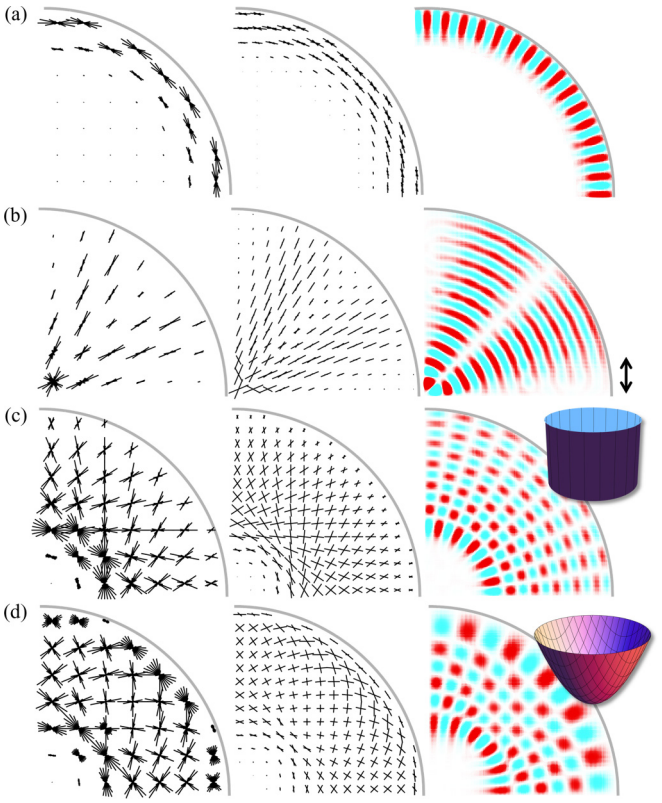

FIG. 2. (Color online) Raw Husimi maps (left), processed Husimi Maps (middle), and the wave function (right) for eigenstates of the circular well (a)–(c) and the harmonic oscillator (d). Double-arrows at far right indicate the spread of the coherent state ($\Delta k/k = 10\%$). The states in (c) and (d) correspond to the classical paths in Figs. 14(a) and 14(b), respectively.

The Husimi vectors in Fig. 2(c) align to suggest straight trajectories, but the vectors in Fig. 2(d) do not, suggesting the presence of curved paths. Moreover, projections near the boundaries of both systems indicate that the paths of the circular well scatter off the boundary with a consistent and acute angle, while for the harmonic oscillator system the trajectories lightly strike the "edge" at the classical turning point position, where a classical particle would return towards the center of the harmonic system for that particular initial energy. As seen in this example, the processed Husimi flow markedly elucidate the dynamics present, but not always apparent in wave functions.

If we center the Husimi projections on points that correspond with the predicted classical paths, clear trajectories can be seen without processing the raw Husimi map. This makes it possible to identify the source of slight deviations from the classical paths that are exhibited towards the center of the system. We explore both issues in Appendix D.

B. Magnetic field

In comparison to the traditional flux, processed Husimi maps extract more information from systems without time-reversal symmetry, such as those in the presence of a magnetic field. To properly represent these states, both the momentum operator in Eq. (1) and the momentum term $i\mathbf{k}_0 \cdot \mathbf{r}_0$ in Eq. (3)

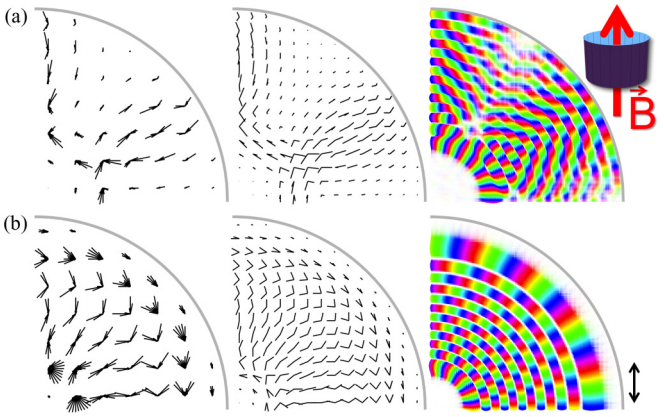

FIG. 3. (Color online) Raw Husimi map (left), processed Husimi maps (middle), and wave function (right) for two eigenstates of the circular well with magnetic field coming out of the plane. The magnetic field strength is set so that the cyclotron radius is approximately 1/2 (a) and 1/3 (b) the radius of the system. Double-arrows at far right indicate the spread of the coherent state ($\Delta k/k = 10\%$). Both states correspond to the classical paths presented in Fig. 4.

must be modified to reflect the canonical transformation

$$\mathbf{p} \rightarrow \mathbf{p} - q\mathbf{A}/c, \tag{7}$$

where the magnetic potential $\mathbf{A}$ is defined in Appendix B.

The circular well states without magnetic field in Fig. 2 exhibit cross-hatching nodal patterns which are absent from the states in the magnetic systems. In the presence of a magnetic field the wave functions (see Fig. 3) exhibit circular nodal patterns with complex phase arguments. The processed Husimi maps for each state indicate circular classical trajectories with radii corresponding to the cyclotron radius. At the magnetic fields used here, the cyclotron radius is smaller than the system size (see Appendix B), as presented in Fig. 3.

Figure 4 present maps of the current flow and the classical trajectories corresponding to the magnetic systems depicted in Fig. 3. The trajectories correlate strongly with the processed Husimi map. Like the circular well states, the presence of multiple trajectories at each point in Fig. 4 can be explained by the intersection of rotated classical trajectories that arise from rotational symmetry. For the state in Figs. 3(a) and 4(a), we have artificially removed rotational symmetry to highlight fewer paths.

The approach of mapping the flow using the flux operator on a wave function is rather unreliable. The flux map in the left column of Fig. 4, obtained by integrating the flux with a Gaussian kernel corresponding to the coherent state used to generate the processed Husimi map, does not follow the classical paths (right column) corresponding to the system. The traditional flux map $\mathbf{j}(\mathbf{r})$ averages over *all* trajectories at each point. As seen in Fig. 4, the particle flow at a point obtained from the flux averages over the two main directions of flow obtained from the processed Husimi. The flux operator fails to indicate the full classical dynamics underlying a quantum wave function. In contrast, the processed Husimi map (middle column of Fig. 4) reproduces the classical paths with remarkable fidelity. The flux is able to instead measure

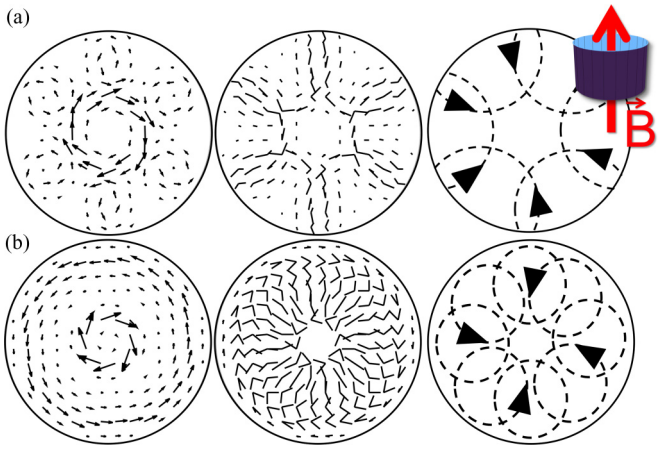

FIG. 4. (Color online) Maps of the flow for the two states presented in Figs. 3(a) and 3(b). (Left) the flux map, (center) the processed Husimi map, and (right) classical paths. The traditional flux correlates strongly with Husimi flux [Eq. (3)] but fails to show the classical paths suggested by the wave function.

the total drift flow, which might be the desired quantity in some circumstances. The total drift flow is also obtained from the summation of all vectors at each point in the processed Husimi map.

C. Processing Husimi maps to determine angular deflection

To identify points along the boundary where path deflections occur, we process the Husimi map to extract a quantity we call angular deflection. In Sec. III D, we demonstrate how processed Husimi maps can provide insight into to the semiclassical underpinnings of quantum wave functions in stadium billiard eigenstates. Of particular interest are boundary reflections, which play a key role in the structure of the wave function and its underlying classical paths.

We begin by considering the Husimi function for one point in k space measured at equally spaced points on a grid that covers the system. The scalar field yields a spatial map of the presence of an individual trajectory angle and fluctuations in the map indicate points where classical paths deflect away from and towards the angle. Summing the results for all wave vectors along the contour line defined by the system energy in the dispersion relation, we can derive a measurement of angular deflection $Q_{\text{ang.}}(\mathbf{r};\Psi)$ written as

$$Q_{\text{ang.}}(\mathbf{r};\Psi) = \int D_{\text{abs.}}(\mathbf{r},\mathbf{k};\Psi) k d^d k. \tag{8}$$

$D_{\text{abs.}}(\mathbf{r},\mathbf{k};\Psi)$ is the Gaussian-weighted absolute divergence of the Husimi map for wave vector $\mathbf{k}$ written as

$$D_{\text{abs.}}(\mathbf{r},\mathbf{k};\Psi) = \int \sum_{i=1}^{d} \left| \frac{\text{Hu}(\mathbf{k},\mathbf{r}';\Psi) - \text{Hu}(\mathbf{k},\mathbf{r};\Psi)}{(\mathbf{r}'-\mathbf{r})\cdot\mathbf{e}_i} \right| \times \exp\left[\frac{(\mathbf{r}'-\mathbf{r})^2}{2\sigma^2}\right] d^d r', \tag{9}$$

where the sum is over the d orthogonal dimensions associated with the appropriate unit vector $\mathbf{e}_i$.

Processing the Husimi map to measure angular deflection has close ties to its initial implementation as a measurement state for building phase diagrams [3]. For instance, it is possible to use the divergence of the Husimi map for each wave vector to compute the quantum analog of a state's Poincare map [9]. This form of the Husimi map has been used to examine the angle of impact against a coordinate along the boundary [9] to study chaotic behavior in stadium billiards [10,11]. Angular deflection can also be used to examine the case where external fields cause path deflection, such as in the presence of a strong magnetic field, although we do not explore such use in this paper.

D. Stadium billiard eigenstates

The classical dynamics of circular stadia are integrable while those of the Bunimovich stadium [12] are chaotic. As a result, the stadium has been featured in many studies of quantum chaology [9,13–19]. In addition, stadium billiards provide another perspective on the utility of the processed Husimi map. Unlike the circular system already presented, where the trajectories accumulating at a particular point are fairly regular and predictable, all points in a stadium billiard eigenstate are rife with many unpredictable trajectories. In this regime, the processed Husimi map validates its use as an ideal tool for lifting the veil on the underlying classical dynamics. This is particularly true once issues regarding the selection of the width parameter σ are addressed, which we discuss in Appendix E.

In Fig. 5, we present raw and processed Husimi maps for three eigenstates of the closed stadium billiard system. For each calculation, the size of the coherent state is kept constant, but because the energy of the eigenstates increases from top-to-bottom, the momentum uncertainty for each Husimi projection also increases. This is reflected in the clarity of the suggested classical paths at higher energy as well as the reduction of angular deflection in the bulk (which exhibits small positive values in the top figure due to uncertainty, not because there is actual deflection at these points).

To the untrained eye, the wave functions in Fig. 5 do not appear to emphasize isolated classical trajectories, the scars found in the high-energy stadium states [11,14,16,17,19], and explored in Appendix E, specifically since at low energies the system only accommodates a few wavelengths along its diameter. In the processed Husimi map, however, it is quite clear that a very limited set of classical trajectories are largely responsible for these wave functions, suggesting that Husimi projections could be used to study the properties of low-energy scar states [2].

Sections with high angular deflection show, which parts of the system boundary are responsible for the creation of each state and indicate where adiabatic changes in the boundary conditions are most likely to affect the state [19,20]. This can be imagined as a quantum force on the boundary. Because the size of the coherent state used to generate each Husimi map is kept constant, the angular deflection penetrates into the bulk to the same extent for each state. However, the locations of high angular deflection along the boundary form a unique fingerprint for each state.

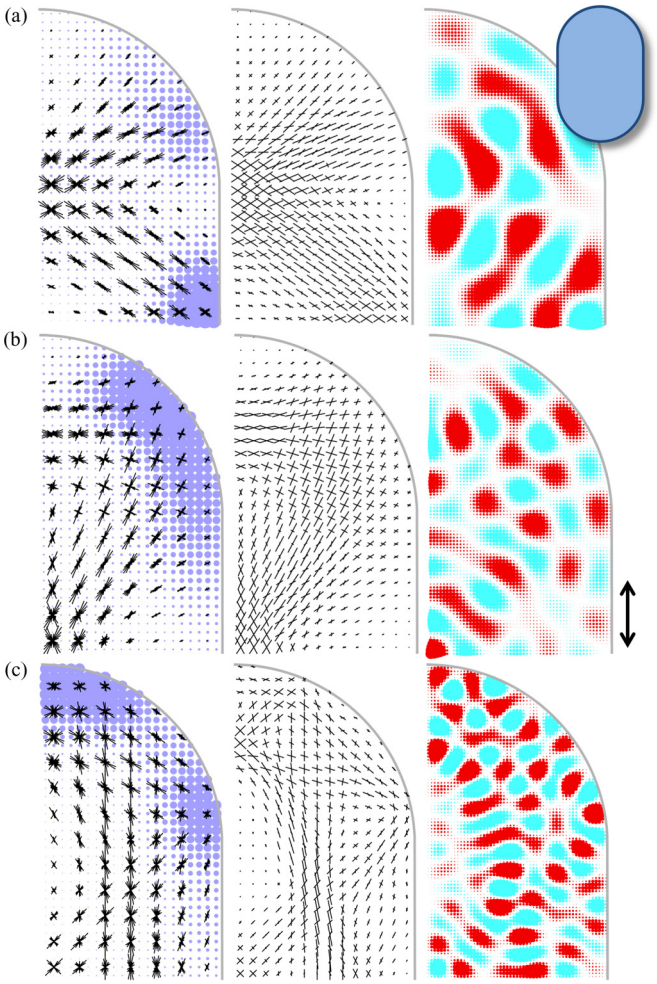

FIG. 5. (Color online) Eigenstates of the stadium billiard system with Dirichlet boundary conditions at three increasing energies, with the raw Husimi map (left), processed Husimi map (middle), and wave function (right). Angular deflection is indicated in blue in the left column. Double arrows indicate the spread of the coherent state used in the calculations [$\Delta k/k = 20\%$ (a), 15% (b), and 10%(c)].

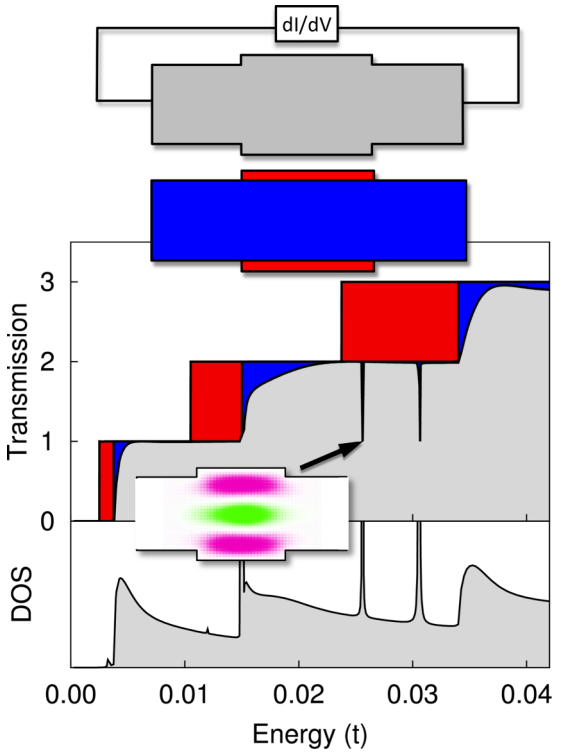

FIG. 6. (Color online) (Top) An infinite waveguide schematic with a slight bulge in the middle (grey). This system can be modeled as two waveguides of different widths (blue and red). (Bottom) In an infinite waveguide, the transmission curve has a series of plateaus as each transverse mode opens up (blue transmission curve). In a wider waveguide, each mode opens up at lower energies (red curve). If only a small segment of the waveguide is widened, then subthreshold resonances occur in between the energies of the narrow and wide waveguides (grey transmission curve). These resonances correlate with subthreshold resonant states, which peak in the density of states (DOS) at those energies. Energy is given in units of t where $4t$ is the band edge.

IV. FLUX THROUGH OPEN SYSTEMS

A. Subthreshold resonance

The previous section used processed Husimi maps to examine the semiclassical dynamics of closed systems directly from their wave functions, providing substantial benefits over the usual flux operator, which vanishes for time reversal symmetric systems, and averages all trajectories (thus missing crisscrossing trajectory paths, see Fig. 4) when a magnetic field is present. Moreover, the spread of the coherent state used to generate the Husimi map provides flexibility to examine dynamics at a variety of scales, while the flux operator is confined to the limit of infinitesimal spread. In its traditional guise [Eq. (1)], the flux operator is most often employed in scattering problems which arise when a closed system is coupled to leads or baths. Is it possible to connect the semiclassical dynamics of the closed system to the open system using an extended Husimi flux?

In this section, we demonstrate how the Husimi flux can help interpret the traditional flux and deepen our understanding of transport across a device. We consider subthreshold resonance for a waveguide that is slightly widened along a short section (see inset, Fig. 6). In an unperturbed waveguide, transport occurs through transverse modes, which open for transport when the system energy exceeds the transverse energy of the mode. At these energies, the transmission function exhibits distinct plateaus as seen in Fig. 6, where the plot of the transmission for a wide(narrow) waveguide is presented in red (blue).

If a section of a narrow waveguide is widened, the transverse energy of each mode diminishes in the wider section. Thus, for each mode, there is a range of energies bounded above by its transverse energy in the unperturbed waveguide, and below by its energy in the wider region. In this energy range, the mode can reside in the wider region but cannot propagate through the narrower leads where it is an evanescent wave. This forces the system into a quasibound state which is trapped in the wider region and is only weakly coupled to the environment, causing a striking peak in the density of states, commonly known as a Feshbach resonance [21]. In the quasibound state, the particle

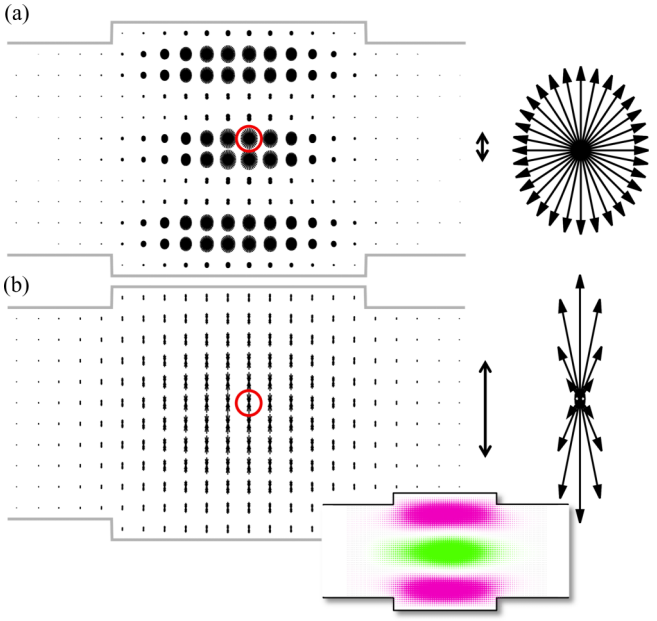

FIG. 7. (Color online) The raw Husimi map for the resonant state (see inset) is plotted using (a) $\Delta k/k = 100\%$ and (b) $\Delta k/k = 20\%$. The spread of the test wave packet is indicated by the respective double-arrows. A single Husimi projection (circled in red) for each map is magnified at right. The vector sums of each map are shown in Fig. 9(b).

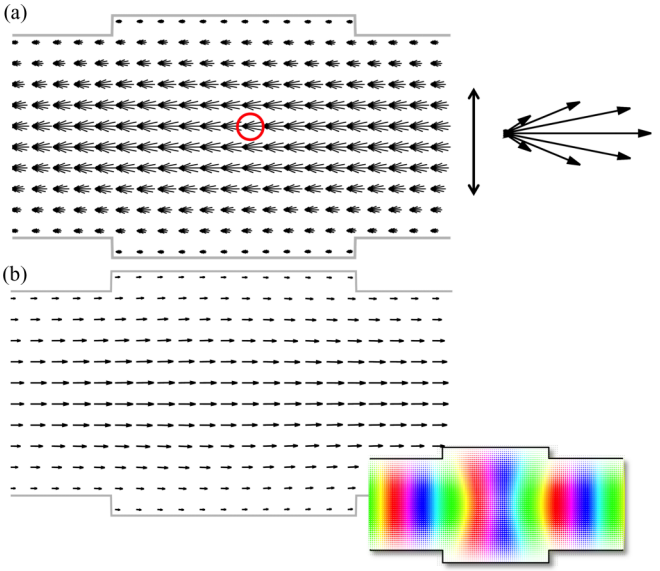

FIG. 8. (Color online) (a) The raw Husimi map for the wave function of the lowest propagating mode (see inset) of the waveguide in Fig. 6. The energy of the state is well above resonance ($E = 0.02745$). The uncertainty for this map is $\Delta k/k = 20\%$. A magnified view of the projection circled in red is presented at right. (b) The Husimi flux. This is the mode that hybridizes with the resonant state to produce Figs. 7 and 9.

bounces vertically between the walls of the perturbed region and is unlikely to escape.

At certain energies, a particle propagating in a lower energy mode corresponding to the narrow section interacts with the wider region and becomes trapped in the quasibound state. This causes the quasibound state to hybridize with the propagating mode and interfere with the transmission in the device, as seen in Fig. 6. The suppression of transmission appears as a pair of sharp dips, accounting for symmetric and antisymmetric versions of the Feshbach resonance. Since the resulting wave function is the hybridized state that inhabits the system at resonance, we refer to it as the resonant state.

We compute the wave function of the resonant state corresponding to the first dip in the transmission shown in Fig. 6 (indicated by the arrow in the transmission function) according to the method outlined in Appendix C. This method allows the extraction of the pure resonant state without the second-lowest propagating mode, which is also present at these energies. Figure 7 shows two raw Husimi maps for this wave function produced using coherent states with uncertainties of $\Delta k/k = 100\%$ and 20%, respectively. Spatial variations in the Husimi map decrease as the size of the coherent state increases, as we present later in Fig. 15.

The raw Husimi map is indistinguishable from the quasibound state and the resonant state, which is expected since the resonant state is only slightly perturbed by the propagating mode. The flux of the quasibound state is zero. Moreover, as the energy is increased across resonance, the wave function does not substantially change in appearance, while the flux patterns alter dramatically. At first, these behaviors appear to contradict the Husimi map, but below we show that the flux patterns correlate with subtle changes in the Husimi maps that can be retrieved by adding all their vectors.

We can begin to understand these subtle changes by examining the lowest propagating mode. The raw Husimi map far away from resonance, shown in Fig. 8 using a moderate size coherent state, corresponds to a complex plane wave with a single wave vector. In the Husimi flux, the left-to-right flow appears unchanged within the central region of the system. The flux operator for this mode, not shown, is similar. In contrast, the vector-sum and the flux of the bound state is always zero. So what happens when it interacts with the lowest propagating mode to produce the resonant state?

In Fig. 9, we address this question by showing the traditional flux, wave function, and the Husimi flux. The energy for each state is (a) above, at (b), and below (c) resonance. The flux operator is integrated over a Gaussian kernel corresponding to a coherent state spread of $\Delta k/k = 100\%$ and is identical to the Husimi flux with the same coherent state spread. In the flux operator, we see the characteristic vortex patterns shift in direction above and below resonance, as expected when the bound state passes through a phase of π over resonance. Moreover, while it is clear that the presence of the lowest propagating mode is stronger away from resonance, the wave-function representation at all three energies are strongly influenced by the bound state. Similarly, probability flux is strongly localized in the center of the system, and it is unclear how the vortices correlate with the fact that transmission for this mode goes to zero on resonance.

In the Husimi flux, however, the correlation is obvious: above and below resonance, vortices cancel out and leave behind the drift velocity of the mode. For these energies, the Husimi flux is quite similar to the lowest propagating mode

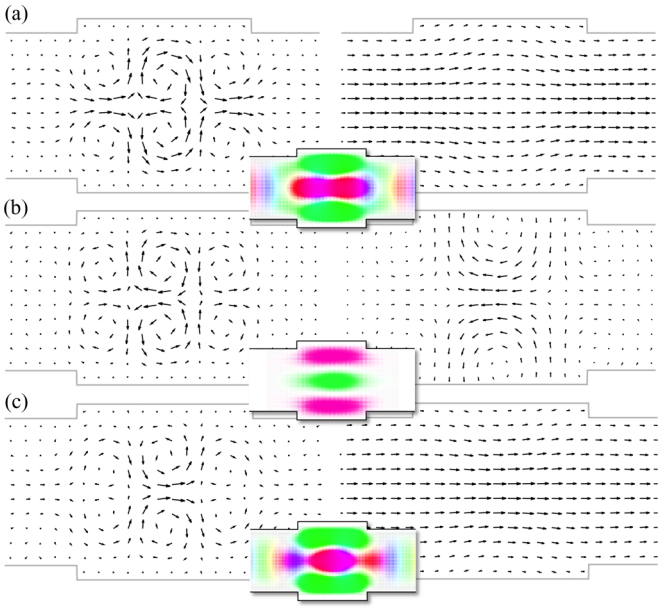

FIG. 9. (Color online) The traditional flux (left column) and the Husimi flux (right column) for the resonance state in Fig. 6 slightly above resonance (a, $E = E_{\text{res.}} + 0.00005$), at resonance (b, $E = E_{\text{res.}}$) and slightly below resonance (c, $E = E_{\text{res.}} - 0.00005$). The coherent state for the Husimi flux corresponds to $\Delta k/k = 0.2$. The transmission function for this mode corresponds to (a) $T = 0.99$, (b) 0.06, and (c) 0.99 for the respective energies. Even though the raw Husimi maps (not shown) at each energy are indistinguishable from Fig. 7, their vector additions (Husimi flux) vary substantially. Energies are in arbitrary units, scaled to Fig. 6.

in Fig. 8, and the left-to-right flow extends through the semi-infinite leads, although there are slight changes in the central region. At resonance, however, the vortices no longer interfere to produce flow from left-to-right, but instead persist as larger vortices across the central region, which counteract the left-to-right flow from the leads, resulting in zero transmission for this mode. The second-lowest propagating mode (not shown), which is antisymmetric along the transverse direction, does not interact with the resonance and maintains full transmission.

At all energies, the raw Husimi map shows the simple vertical bouncing trajectories that are identical to the bound state (Fig. 7), while the left-to-right flow of the lowest propagating mode (Fig. 8) interferes with these paths to produce the residual flux vortices. The classical dynamics of the resonance therefore indicate a subtle shift in the overall contribution of classical trajectories that give rise to the resonance. Because the vertical trajectories can easily cancel each other out, the residual becomes exquisitely sensitive to the initial conditions of such classical paths, which are determined solely by the energy of the lowest-propagating mode.

Examining this system using the Husimi flux allows us to extract details at small spreads similar to the information found using the flux operator. Yet, the Husimi flux also can indicate larger drift flows when utilizing larger spreads. Important information about the resonance can be retrieved at all scales, since the flow can be understood as the slight residuals of the full Husimi projection found at different coherent state spreads. By adding the Husimi projection and the Husimi flux to the wave analysis tool set, we can examine the problem at various scales and construct a more nuanced and complete story.

B. Transport through complex geometries and the nature of flux vortices

In the previous section, we explored different scales of flow patterns by varying the spatial spread of the coherent states (σ) used to generate a Husimi map. In this section, we vary the σ parameter to reveal the behavior of the probability flux at arbitrary scales in systems with geometries more complex than a simple waveguide: a square system with two small leads and a half stadium with two attached leads.

In the square system, the size of the square is much larger than the characteristic wavelength at the energies of interest. The leads are displaced vertically from the center towards the bottom-left and upper-right corners. Further, there is an obstruction in the middle of the system that constrains transport towards the central region. As a result, transmission in this device requires that particle trajectories must reflect off the boundaries several times.

In Fig. 10, we present a scattering state wave function for this system, a magnified view of the traditional flux, the Husimi flux, and the processed Husimi map. The scattering wave function [see Fig. 10(a)] acts as a mode of unit transmission for a square system with two small leads. The nodal lines appear along the 45° diagonals, which is corroborated by trajectories favoring those diagonals in the processed Husimi map [see Fig. 10(c)]. This arises because all boundary conditions are vertical or horizontal walls; since each mode of the unperturbed waveguide leads is associated with a distinct pair of trajectory angles, the vertical and horizontal walls therefore reflect all trajectories back onto the same pair rotated at 45°. At the energy selected, the pair of trajectory angles for the incoming mode are at perfect 45° diagonals, so that their rotations from reflecting off the walls also point along the diagonals, resulting in standing wave patterns.

The Husimi flux [see Fig. 10(b)] for this state presents a conductance pathway where it is clear that transport follows primarily through a narrow channel. Here, most of the particle flow is from the lower-left to the upper-right corners. By comparison, the traditional flux map (not shown) is rife with vortices throughout the entire system, dramatically limiting our ability to identify overall flow. The conductance pathway does not have to be classical, since it is an aggregate phenomenon formed from many trajectories; as a result, it is able to curl in the bulk without external forces, as seen in Fig. 10(b). Pairs of vortices form as the pathway moves from the central part of the device towards the region where perpendicular classical paths (indicated by the processed Husimi map) dominate. We highlight one such region with a black box and present in the inset of Fig. 10 the traditional flux for this region. These vortex pairs are a direct analog to those found in subthreshold resonance as the left-to-right conductance pathway passes through perpendicular trajectories in the perturbed waveguide (see Fig. 9 and the surrounding discussion).

We now proceed to another complex geometry (see Fig. 11) and examine a full-transmission scattering state for a large

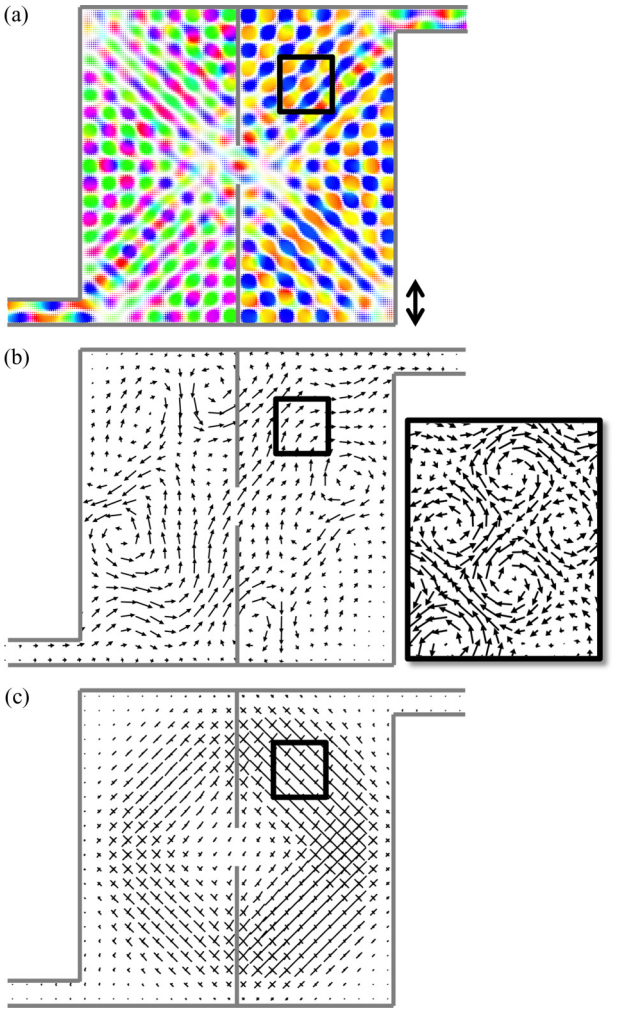

FIG. 10. (Color online) A scattering wave function associated with full transmission through a partially obstructed square device. (a) Wave function of the system, (b) the Husimi flux, and (c) the processed Husimi map. The coherent state spread used is $\Delta k/k = 10\%$, indicated by the double arrows. The inset shows the traditional flux over the part of the system indicated by the black squares.

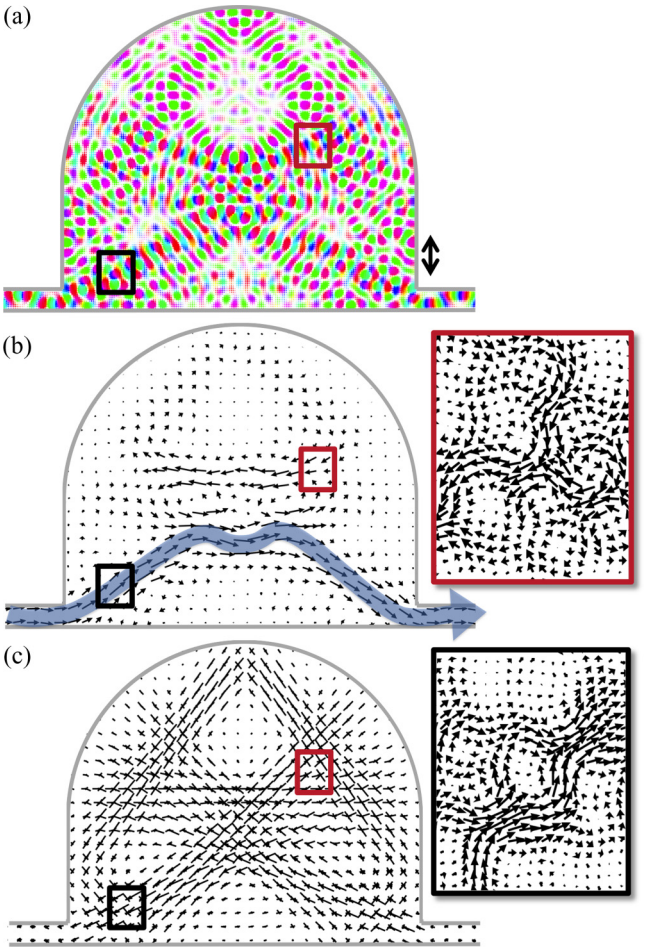

FIG. 11. (Color online) A scattering wave function associated with full transmission through the half-stadium. (a) Wave function representation, (b) the Husimi flux, and (c) the processed Husimi map. The coherent state spread used is $\Delta k/k = 10\%$, indicated by the double arrows. Black and red squares highlight regions of particular interest (see text). The traditional flux from the respective highlighted regions of the system is shown magnified in the insets.

half-stadium with two leads attached at its sides. Given that scar orbits must self-loop but be otherwise unstable [2], scar states can only participate in transport when the leads attach at points that are slightly displaced from one of the orbit's reflection points; otherwise, the classical orbit leaks out the system too quickly. The wave function in Fig. 11 shows strong scarring, and the processed Husimi map corroborates the scarring with an identifiable classical orbit which just misses the leads.

Like the partially obstructed square device in Fig. 10, the traditional flux also occurs most strongly along a narrow conductance pathway which, in this case, flows along the bottom of the device while deviating into the bulk at its middle. In addition, flux vortices occur throughout the system, making interpretation of the dynamics difficult without applying our methods. In contrast with the square device, these vortices no longer form identifiable pairs. In the half-stadium state, classical paths do not intersect at 90° angles, but take on a range of oblique angles. As a result, the vortices take on forms that are consistent with the processed Husimi map at each intersection. For instance, in the black inset, there is strong flow from bottom left to upper right, with other near-vertical flows forming vortices. In the red inset, there are three primary flows propagating at 60° to each other, forming the triangular arrangement of vortices shown.

V. CONCLUSIONS

The processed Husimi map algorithms for the visualization and extraction of the dynamics of wave functions presented here are powerful tools. They provide an extremely accurate way to reveal the dynamics and classical ray structures of a quantum wave function. Also, this technique can be used in a wide variety of systems and to calculate properties such as angular deflection, boundary reflections, and the flux. The results and examples presented in this paper demonstrate the technique as invaluable for informing a design principle in quantum systems, since it provides a map of how boundaries affect individual quantum states (Sec. III D), as well as the

impact of potentials (Sec. 2), and magnetic fields (Sec. III B). In addition, we have shown its utility for illuminating the phenomena underlying resonance when a closed system interacts with an environment (Sec. IV A), while explaining the source and properties of flux vortices (Sec. IV B). Because of its ability to contextualize the flux operator and identify the primary conductance pathway in large systems, the processed Husimi map is an ideal tool for interpreting quantum conductance simulations.

This paper focuses on two-dimensional systems, since they are ideal for demonstrating the significant physical intuition that the Husimi tools are able to provide. However, its definition is not limited to such systems. It is equally well suited to three-dimensional systems, and may be able to provide a significant contribution to interpreting molecular orbitals, augmenting such technologies as Bader surfaces analysis [22] and local currents [23].

ACKNOWLEDGMENTS

M.F.B. and E.J.H. gratefully acknowledge funding from the U.S. Department of Energy, Office of Basic Science under Award No. DE-FG02-08ER46513. D.J.M. acknowledges support from the U.S. Department of Energy, Computer Science Graduate Fellowship program No. DE-FG02-97ER25308.

APPENDIX A: UNCERTAINTY PROPAGATION FOR HUSIMI VECTOR ADDITION

When integrating over the available k space in Eq. (3), the resulting Husimi flux vector has lower uncertainty than the individual terms in the integral, but by how much? Understanding this detail is key to appreciating why the Husimi projection is valuable when extending the flux operator to an operator with defined uncertainty. Moreover, understanding the behavior of uncertainty propagation in this integral makes it possible to confidently approximate the result with a discrete sum, offering both visual and computational advantages.

We begin by considering the extreme cases. If the wave vector orientation remains unchanged for each measurement, summing up identical measurements has no effect on the final relative uncertainty. On the other hand, when either the spatial coordinates or the wave vectors are sufficiently separated, each Husimi vector constitutes an independent measurement; the uncertainty of the result will reduce by the square root of the number of measurements. In general, calculations fall in between these two extremes. This analysis is performed in only one dimension since to obtain the variance in more than one dimension we would just need to add the variance along each orthogonal axis. First, the coherent state is expressed in the momentum basis as

$$\langle \mathbf{k}|\mathbf{r}_0,\mathbf{k}_0,\sigma\rangle = \left(\frac{2\sigma}{\sqrt{\pi/2}}\right)^{1/2} e^{-\sigma^2(\mathbf{k}-\mathbf{k}_0)^2+i(\mathbf{k}-\mathbf{k}_0)\cdot\mathbf{r}_0}. \quad \text{(A1)}$$

Most generally, the Husimi projection in Eq. (3) is the integral of Husimi functions over all of k space. In this appendix, and in the figures throughout this paper, the integral is replaced with a finite sum of test wave vectors $\{\mathbf{k}_i\}$, which satisfy the dispersion relation at a particular energy.

The variance of the integral in Eq. (3) (the vector-valued Husimi flux) can be obtained by building on intuition about coherent states. The k-space variance of the coherent state can be derived by integrating the coherent state probability amplitude over k-space, weighting the integrand by $(\mathbf{k}-\mathbf{k}_0)^2$. Using the notation in Eq. (A1), this gives $\sigma_k^2 = \frac{1}{4\sigma_x^2}$, where σ_k and σ_x are the spread in momentum and real space of the coherent state. The properties of coherent state yield the relation $\sigma_x\sigma_k = \frac{1}{2}$. This can be thought of in the Husimi formulation as a statistical result where the quantity σ_k is the variance of each individual term in the Husimi vector summation. In this representation, the variable is the wave vector and the probability function is the probability amplitude of the coherent state. Because the probability function is complex, we take the absolute sum squared.

Factoring in more than one Husimi function into the Husimi projection results in the expression

$$\frac{2\sigma}{\sqrt{\pi/2}}\int_{-\infty}^{\infty}\left|\sum_i (k-k_i)e^{-\sigma^2(k-k_i)^2+i(k-k_i)x_0}\right|^2 dk, \quad \text{(A2)}$$

where the integral is over the set $\{\mathbf{k}_i\}$ of test wave vectors, projected onto the given axis, x_0 is the spatial point being tested, and σ is the chosen spatial Gaussian spread. By setting the coherent states to the same phase at their centers, $x_0 = 0$, the above integral can be evaluated and the spread in momentum is

$$\sigma_k^2 = \frac{1}{4\sigma^2}\left[N + 2\sum_{i,j>i} e^{-\frac{\sigma^2}{2}(k_i-k_j)^2}(1-\sigma^2(k_i-k_j)^2)\right]. \quad \text{(A3)}$$

Already it is possible to test this result against intuition. If each wave vector is identical, then $k_i - k_j = 0$ and the sum of N measurements results in the uncertainty $\sigma_k^2 = \frac{N^2}{4\sigma^2}$ which would provide no reduction of relative uncertainty. When $|k_i - k_j| \gg \sigma$, the exponential term will overwhelm the quadratic term and the uncertainty becomes $\sigma_k^2 = \frac{N}{4\sigma^2}$, a reduction in the relative uncertainty of $\sqrt{N}$.

The second term in Eq. (A3) quantifies the covariance between measurements. In Fig. 12, we plot this quantity for two vectors which can actually be negative. The lower bound of $Q(k_1,k_2,\sigma) = 2e^{-\frac{\sigma^2}{2}(k_2-k_1)^2}(1-\sigma^2(k_2-k_1))$ is $-\frac{4}{e^{3/2}} \approx -0.893$, achieved at $|k_2-k_1| = \sqrt{3}/\sigma$.

The terms in Eq. (A3) suggest that when additional vectors are added, the uncertainty can be reduced arbitrarily by setting the correct separations between the test wave vectors (Q is zero for some vector combinations). It even suggests that for three or more vectors we could possibly produce results with negative uncertainty, but intuitively that cannot be possible. To appreciate why, Fig. 13 plots the results of σ_k^2 for the addition of three wave vectors.

The minima that occur from maximizing the separation between each pair of wave vectors is indicated by the white dashed lines. At the center of the graph, a peak exists at $\sigma_k^2 = 9/4\sigma^2$, which falls to $3/4\sigma^2$ for regions beyond the area bounded by the white dashed lines, consistent with earlier observations. There is also a minimum (positive) uncertainty

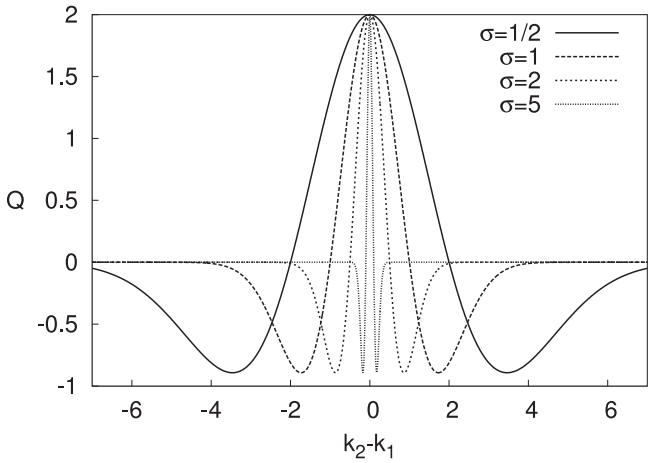

FIG. 12. The second term in Eq. (A3) is plotted for the addition of two vectors in the Husimi projection. This term represents the covariance between the two vectors, and is bounded above by 2 and below by $-\frac{4}{e^{3/2}}$ for all choices of σ.

arising from the fact that the separation between all pairs of points on a line cannot be equal. as shown in Fig. 13 where there are no points where three dashed lines intersect. For two vectors the minimum occurs at $\sigma_k^2 \approx 0.981/4\sigma^2$, for three $\sigma_k^2 \approx 1.017/4\sigma^2$, and for four $\sigma_k^2 \approx 1.036/4\sigma^2$. We can generalize and state that for $N_{\min}$ vectors that fall on separate minima, the uncertainty of their sum will be $\sigma_k \approx \frac{1}{2N_{\min}\sigma}$. Moreover, even if vectors are added that do not fall on the uncertainty minima in Figs. 12 and 13, they will have a negligible impact on the total relative uncertainty. To summarize, no matter how many vectors contribute to the sum, only the vectors on the minima will reduce the relative uncertainty. This shows that the key quantity is not the total number of vectors that are added, but the number that have sufficient separation to fall on the uncertainty minima.

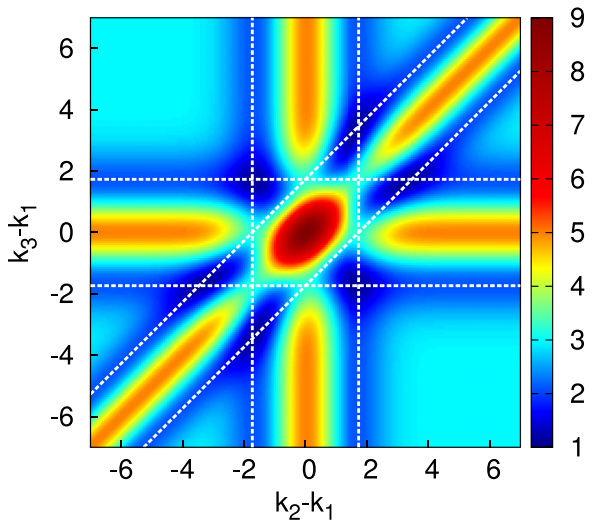

FIG. 13. (Color online) Uncertainty obtained by summing three vectors of a Husimi projection, as written in Eq. (A3). The uncertainty is bounded above by $9/4\sigma^2$ and below by $\sim 1.017/4\sigma^2$. The dashed white lines indicate local minima that result from spacing each pair of vectors by $\sqrt{3}/\sigma$, which would give a minimum uncertainty for two-vector addition (see Fig. 12).

How many vectors is this? We know, for instance, that this minimum occurs when the maximum number of vector pairs has a separation near $\sqrt{3}/\sigma$. Further, this is likely to occur when the vectors are evenly spaced on a line at that separation. Thus we propose that the number of vectors that can fall on the minima is given by $N_{\min} = \text{floor}(2k(E)\sigma/\sqrt{3})$, and using $\hbar k = \sqrt{2mE}$, we can rewrite this as $N_{\min} = \text{floor}(\sigma\sqrt{\frac{8mE}{3\hbar^2}})$. Substituting this value results in the proportionalities

$$\Delta k/k \propto \frac{1}{N_{\min}\sigma} \propto \left(\frac{\sigma}{\hbar}\sqrt{mE}\right)^{-1}. \tag{A4}$$

This makes sense intuitively: the relative uncertainty of a finely sampled Husimi vector addition goes down with larger σ and energy.

This result deepens the connection between the flux operator and the Husimi function for small σ, since for very small coherent states, the uncertainty minima, which are separated by σ^{-1}, grow increasingly far apart. There is only a finite range of wave vectors that satisfy the dispersion relation at a given energy, meaning that as the coherent states get smaller, fewer and fewer samples in k-space minimize the uncertainty. In fact, at the extreme limit of $\sigma \to 0$, the uncertainty cannot be minimized beyond a single measurement in each orthogonal direction, indicating that results for these small coherent states have undefined uncertainty, just like the flux operator. An alternative proof of this result can be found in Mason *et al.* [1].

APPENDIX B: THE HAMILTONIAN

The numerical simulations presented in this paper use a free-particle Hamiltonian $H = -\frac{p^2}{2m} + U(\mathbf{r})$ sampled on a square grid with spacing a and where $U(\mathbf{r}) = 0$ at all points unless otherwise stated. This Hamiltonian can be expressed in more familiar language by using the tight-binding approximation. The effective mass envelope function Hamiltonian becomes $H = \sum_i \epsilon_i \mathbf{a}_i^\dagger \mathbf{a}_i - t\sum_{\langle ij\rangle} \mathbf{a}_i^\dagger \mathbf{a}_j$, where $\mathbf{a}_i$ is the annihilation operator for the i^{th} site, ϵ_i is the energy of the system plus the disorder potential, and the set $\langle ij\rangle$ cycles through all nearest-neighbor pairs. The hopping term is $t = \frac{\hbar^2}{2ma^2}$ and $\epsilon_i = 4t + U_i$, where U_i is zero unless otherwise stated.

Section III B uses the Peierls substitution [24] to incorporate magnetic fields, using the language of the tight-binding model. The magnetic field contributes a phase to the hopping potential t:

$$t_{ij} = t\exp[i\phi], \phi = q\mathbf{A}\cdot(\mathbf{r}_i - \mathbf{r}_j)/\hbar, \tag{B1}$$

where $\mathbf{r}_i$ is the position vectors of the site corresponding to the ith column of the Hamiltonian, $\hbar$ is Planck's constant, and q is the electron charge. Calculations in this paper assume that the magnetic field is perpendicular to the plane on which the system sits and is bounded by a cylinder centered on the system's center. The radius of this column is chosen to be greater than the size of the system. Accordingly, the gauge of the magnetic potential for an out-of-plane magnetic field is defined such that

$$\mathbf{A}(\mathbf{r}) = \frac{\mathbf{e}_\theta}{2\pi r}\int B_z dx dy, \tag{B2}$$

where the integral is over a disk centered on the origin and limited by radius r.

The cyclotron radius can be determined by the following relation:

$$r = \frac{\hbar k}{B_0 q}. \tag{B3}$$

For a free particle, $\hbar k = \sqrt{2mE}$, giving

$$\frac{r}{a} = \frac{\sqrt{2mE}}{B_0 q a^2}. \tag{B4}$$

This means that at $E = 0.2\frac{\hbar^2}{ma^2}$, the energy used in Sec. III B, a magnetic field strength of $B = 2 \times 10^{-3}\frac{\hbar}{qa^2}$ is sufficient to produce a cyclotron radius that is 2/3 of the system radius.

APPENDIX C: SCATTERING WAVE FUNCTIONS

Diagonalizing the Hamiltonian to examine eigenstates of a closed system is straightforward. Section IV A, however, examines an open system in a standard ballistic conductance calculation. The numerical Green's function formalism is used to obtain the scattering wave function for these calculations, for which modern implementations are outlined in several texts [25–27]. In this formalism, the Hamiltonian is divided into a left-lead, central region, and right-lead projections

$$H = \begin{pmatrix} H_L & V_{LC} & 0 \\ V_{LC}^\dagger & H_C & V_{RC} \\ 0 & V_{RC}^\dagger & H_R \end{pmatrix}. \tag{C1}$$

The semi-infinite Green's function at the surface of each lead is calculated using the Lopez-Sancho method, $g_{L,R}(E)$ for the left (L) and right (R) (identical) leads. To compute the complete Green's function, the device $G(E)$ and the semi-infinite surface Green's functions $g(E)$ for each lead [28,29] are first computed and matched to the surface Green's function of the device region, using the numerical technique outlined in Mason *et al.* [30].

The coupling matrix for the left lead to the central region is then defined by $\Gamma_L(E) = 2\mathrm{Im}[V_{LC}^\dagger g_L(E) V_{LC}]$. This results in a density matrix of coherent scattering wave functions $\rho(E) = G(E)\Gamma_L(E)G(E)$. Each coherent scattering wave function in the system can be obtained by diagonalizing ρ. Associated with each eigenvector of ρ will be an eigenvalue equal to the likelihood of measuring the wave function within the system. Since there are generally more basis sets within the central region than modes available to the system through the semi-infinite leads, the vast majority of the eigenvalues will be zero, and the number of nonzero eigenvalues will be equal to the number of modes available to the system at the given energy. This number determines the maximum transmission across the device.

Since a resonant state "traps" the wave function at a specific energy, it creates a striking peak in the density of states. As a result, the resonant state can be easily identified among the eigenvectors of the density matrix since it will be associated with the largest eigenvalue near the resonance energy. When discussing resonant wave functions, it is assumed that we are using a density matrix near the resonance energy and examining the eigenvector associated with the largest eigenvalue (and measurement probability) at that energy. This makes it possible to distinguish the resonant wave function from the ones that are propagating through the system but are unaffected by the resonance.

APPENDIX D: CONSIDERATIONS REGARDING THE MULTIMODAL ALGORITHM AND CLASSICAL PATHS

Processing the Husimi map makes it possible to produce robust visualizations of the underlying classical paths. It is possible to sample the Husimi projections at equally-spaced points along a grid to produce plots. It is also possible to compute quantities such as the angular deflection described in Sec. III C. However, if we instead sample along one of the classical paths that correlate with regions of high density in the wave function, the processing is not necessary since we find a set of Husimi vectors which align themselves perfectly with the classical path. We show these two approaches in Figs. 14(a) and 14(b), which correspond to the wave functions in Figs. 2(c) and 2(d), respectively.

Each Husimi projection in Fig. 14(b) contains an additional set of Husimi vectors which do not align with the path.

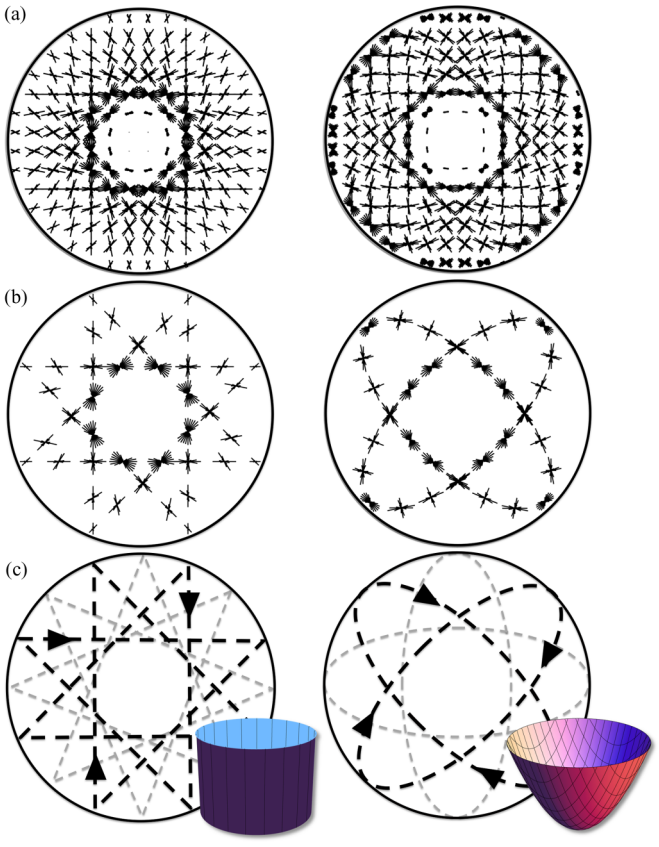

FIG. 14. (Color online) Quantum-classical correspondence from Husimi maps by sampling along classical trajectories. In part (a), the Husimi map for the two eigenstates in Figs. 2(c) and 2(d), where Husimi projections are sampled along a grid. In part (b), projections are instead sampled along classical paths that correspond to the wave function. Because of rotational symmetry, however, the wave function is actually created by the sum of many rotations of such paths, as indicated in part (c).

These vectors can be understood by considering that wave functions for the circular well and harmonic oscillator actually correspond to infinitely many such paths rotated in space due to the circular symmetry of these systems, which we indicate in Fig. 14(c). The "cross-hatching" patterns in Figs. 14(a)–14(b) arise because two rotated classical paths intersect at any point.

Towards the center of the system, a large number of paths come into close proximity. Even though an infinitesimal point is intersected by only two paths, the finite spread of the coherent state is sensitive to other paths nearby, giving rise to Husimi projections showing a large number of trajectories with similar angles. These points in a wave function can violate assumptions of the multimodal algorithm used to process the Husimi map [1], since the different trajectory angles cannot be resolved by the finite spatial and momentum uncertainties of each Husimi projection. As a result, the processed Husimi maps at the centers of Figs. 2(c) and 2(d) show slight deviations from the classical path. The processed Husimi maps show the average classical trajectory at that point and approximations on both sides of the average.

APPENDIX E: CONSIDERATIONS REGARDING THE WIDTH PARAMETER σ

We begin by examining raw Husimi projections for stadium billiard eigenstates, to demonstrate their sensitivity to the width parameter σ. This sensitivity has meaning. Figure 15 shows three Husimi maps for a billiard eigenstate. The wavelength at the energy of the eigenstate is much shorter than the size of the system, allowing well-defined scars to form, which are spawned by modestly unstable and infinitely rare (among all the chaotic orbits) classical periodic orbits [2].

In Fig. 15(a), an extended coherent state is used to generate the raw Husimi map, so that many fine features of the wave function are washed out. Only the scar path (seen as a rotated "v" pattern in the depiction) is clearly visible. The sharply peaked Husimi sunburst reflects both the low momentum uncertainty of the Gaussian used and the strong dominance of the periodic orbit pathway in the eigenfunction.

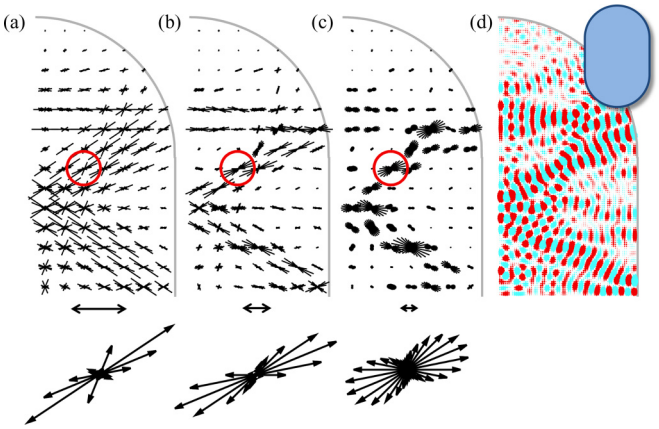

FIG. 15. (Color online) Raw Husimi maps for the scarred stadium billiard eigenstate. Each map uses a different spread of the measurement wave packet. The spread is indicated by the double-arrows on the bottom, with relative uncertainties of $\Delta k/k = 5\%$(a), 20%(b), and 50%(c). A single Husimi projection, circled in red, is magnified at the bottom of each representation.

Compare this to the Husimi map in Fig. 15(c) which is generated by a small coherent state with larger momentum uncertainty. Here, each Husimi projection is more ambiguous, and local variations in the wave function probability amplitude have a large impact on the representation since they are no longer smoothed over. As a result, the trajectories implied by the map no longer continue from one projection to its neighbors and appear somewhat irregular. In general, a compromise can be made by choosing an intermediate momentum uncertainty, as shown in the Husimi map presented in Fig. 15(b). Trajectories are fairly well-resolved, and local variations are easy to follow. Coherent states of this size provide the clearest representation of semiclassical paths.

[1] D. J. Mason, M. F. Borunda, and E. J. Heller, Quantum flux and reverse engineering of quantum wave functions, Europhys. Lett. **102**, 60005 (2013).
[2] E. J. Heller, Bound-state eigenfunctions of classically chaotic Hamiltonian systems: Scars of periodic orbits, Phys. Rev. Lett. **53**, 1515 (1984).
[3] K. Husimi, Some formal properties of the density matrix, Proc. Phys. Math. Soc. Jpn. **22**, 264 (1940).
[4] D. J. Mason, M. F. Borunda, and E. J. Heller, Semiclassical deconstruction of quantum states in graphene, Phys. Rev. B **88**, 165421 (2013).
[5] E. J. Heller, *Wavepacket Dynamics and Quantum Chaology*, edited by M. J. Giannoni, A. Voros, and J. Zinn-Justin, Proceedings of the 1989 Les Houches Summer School on "Chaos and Quantum Physics" (Elsevier Science, North-Holland, 1989), pp. 546–663.
[6] P. W. O'Connor and S. Tomsovic, The unusual nature of quantum Baker's transformation, Ann. Phys. **207**, 218 (1991).
[7] M. S. Child, G. Bruun, and R. Paul, Short time quantum phase space dynamics at a 1:2 Fermi resonance, Chem. Phys. **190**, 373 (1995).
[8] R. W. Robinett, Visualizing the solutions for the circular infinite well in quantum and classical mechanics, Am. J. Phys. **64**, 440 (1996).
[9] M. C. Gutzwiller, *Chaos in Classical and Quantum Mechanics*, Interdisciplinary Applied Mathematics (Springer-Verlag, New York, 1990).
[10] L. Kaplan and E. J. Heller, Measuring scars of periodic orbits, Phys. Rev. E **59**, 6609 (1999).
[11] W. E. Bies, L. Kaplan, M. R. Haggerty, and E. J. Heller, Localization of eigenfunctions in the stadium billiard, Phys. Rev. E **63**, 066214 (2001).
[12] L. A. Bunimovich, On ergodic properties of certain billiards, Funct. Anal. App. **8**, 254 (1974).
[13] M. V. Berry, The Bakerian lecture, 1987: Quantum chaology, Proc. R. Soc. A **413**, 183 (1987).

[14] P. W. O'Connor and E. J. Heller, Quantum localization for a strongly classically chaotic system, Phys. Rev. Lett. **61**, 2288 (1988).

[15] M. V. Berry, Quantum chaology, not quantum chaos, Phys. Scripta **40**, 335 (1989).

[16] S. Sridhar and E. J. Heller, Physical and numerical experiments on the wave mechanics of classically chaotic systems, Phys. Rev. A **46**, R1728(R) (1992).

[17] S. Tomsovic and E. J. Heller, Long-time semiclassical dynamics of chaos: The stadium billiard, Phys. Rev. E **47**, 282 (1993).

[18] F. P. Simonotti, E. Vergini, and M. Saraceno, Quantitative study of scars in the boundary section of the stadium billiard, Phys. Rev. E **56**, 3859 (1997).

[19] A. Barnett, D. Cohen, and E. J. Heller, Deformations and dilations of chaotic billiards: Dissipation rate, and quasiorthogonality of the boundary wave functions, Phys. Rev. Lett. **85**, 1412 (2000).

[20] D. Cohen, A. Barnett, and E. J. Heller, Parametric evolution for a deformed cavity, Phys. Rev. E **63**, 046207 (2001).

[21] H. Feshbach, Unified theory of nuclear reactions, Ann. Phys. **5**, 357 (1958).

[22] R. F. W. Bader, *Atoms in Molecules: A Quantum Theory* (Oxford University Press, New York, 1990).

[23] G. C. Solomon, C. Herrmann, T. Hansen, V. Mujica, and M. A. Ratner, Exploring local currents in molecular junctions, Nat. Chem. **2**, 223 (2010).

[24] R. Peierls, Zur Theorie des Diamagnetismus von Leitungselektronen, Z. Phys. A **80**, 763 (1933).

[25] S. Datta, *Electronic Transport in Mesoscopic Systems* (Cambridge University Press, Cambridge, 1997).

[26] S. Datta, *Quantum Transport: Atom to Transistor* (Cambridge University Press, New York, 2005).

[27] D. K. Ferry and S. M. Goodnick, *Transport in Nanostructures*, Cambridge Studies in Semiconductor Physics and Microelectronic Engineering (Cambridge University Press, Cambridge, 1999).

[28] M. P. Lopez-Sancho, J. M. Lopez Sancho, and J. Rubio, Quick iterative scheme for the calculation of transfer matrices: Application to Mo (100), J. Phys. F: Met. Phys. **14**, 1205 (1984).

[29] M. P. Lopez-Sancho, J. M. Lopez Sancho, and J. Rubio, Highly convergent schemes for the calculation of bulk and surface Green functions, J. Phys. F: Met. Phys. **15**, 851 (1985).

[30] D. J. Mason, D. Prendergast, J. B. Neaton, and E. J. Heller, Algorithm for efficient elastic transport calculations for arbitrary device geometries, Phys. Rev. B **84**, 155401 (2011).